

Impact Experiments on Porous Icy-Silicate Cylindrical Blocks and the Implication for Disruption and Accumulation of Small Icy Bodies

Masahiko Arakawa

Institute of Low Temperature Science, Hokkaido University, Kita-ku Kita 19 Nishi 8, Sapporo 060-0819 Japan
E-mail: arak@lowtem.hokudai.ac.jp

Jacek Leliwa-Kopystynski

Institute of Geophysics, University of Warsaw, ul. Pasteura 7, 02-093 Warsaw, Poland; and Space Research Center of Polish Academy of Sciences, ul. Bartycka 18A, 00-716 Warsaw, Poland

and

Norikazu Maeno

Institute of Low Temperature Science, Hokkaido University, Kita-ku Kita 19 Nishi 8, Sapporo 060-0819 Japan

Received December 24, 2001; revised April 16, 2002

Impact strength and cratering ejecta were studied for porous targets of pure ice and icy-silicate mixture in order to clarify the accumulation and destruction (shattering) condition of small icy bodies. The icy projectile impacted on the cylindrical targets with the porosity up to 55% at a velocity of 150 to 670 m/s at -10°C . The porosity dependence of the impact strength and that of the maximum ejecta velocity were measured in each type of these targets. As a result, the maximum ejecta velocity normalized by the impact velocity ($V_{e\text{-max}}/V_i$) is found to depend only on the porosity (ϕ), irrespective of the target type; a relationship is derived to be $V_{e\text{-max}}/V_i = -2.17\phi + 1.29$. The impact strength of pure ice increased with increased target porosity, but that of mixture target had an opposite trend; that is, the strength decreased with increased porosity. These porosity dependencies of the impact strength could be explained by the porosity dependence of the physical parameters such as impact pressure, pressure decay, and static strength. Finally, the accumulation of small icy bodies is discussed to show that the collisional events can be divided into three types by the porosity and the collision velocity according to our experimental results: mass loss, rubble pile formation, and regolith formation (compaction). © 2002 Elsevier Science (USA)

Key Words: accretion; cratering; ices; impact processes; satellites, general.

1. INTRODUCTION

Recent explorations by spacecrafts have revealed that small asteroids are very porous, with the structure of rubble pile: these porosities are as much as 40–60% (Britt and Consolmagno 2001). Mathilde, one of these porous asteroids, was recently explored in the NEAR mission and an unusually large impact

crater, whose size is 1.24 as large as the radius, was discovered on the asteroid. Unusually large impact craters are observed not only on Mathilde but also on other small asteroids and satellites. Fujiwara *et al.* (1993) found that the curvature of an impacted surface on a small body affected crater shape and the increase in the curvature caused the larger crater radius. Therefore, they thought that small bodies have relatively large craters compared to larger bodies. In addition to this geometrical effect on the crater size, porosity could play an important role in large crater formation.

To study craters on small porous bodies, several experiments related to Phobos and Mathilde have been conducted. Kawakami *et al.* (1991) performed impact experiments on a gypsum target simulating Phobos and studied the impact origin of grooves radially growing from a central large crater, Stickney. They noticed that core-type fractures did not occur even at high-velocity impact on a gypsum target, which means that a strong shock wave associated with high-shock stress causing spallation on a free surface was not excited in the gypsum target because of low-shock impedance and rapid attenuation of shock pressure during the propagation. Thus, they concluded that fracture mode was highly dependent not only on impact velocity but also on the target material properties, especially the porosity. Housen *et al.* (1999) proposed a new mechanism of forming a large crater on a porous body according to their impact experiments on a simulated regolith. They found that the crater formed as a result of the compaction of a porous layer, but not excavation and ejection of impacted material. This new perspective accounted for small amounts of ejecta excavated from craters on small porous bodies like Mathilde. Arakawa *et al.* (2000) performed impact experiments on porous mixtures of H_2O ice– CO_2

ice–pyrophyllite. These targets had thermally stratified structure due to illumination of the sample by the solar-simulating energy flux: The sublimation processes modify the medium and form the stratified structure because the initially uniform sample loses the volatiles (H_2O ice and CO_2 ice), and the sublimation of any particular ice depends on depth (Kossacki *et al.* 1997). They found that the resultant crater size was less sensitive to the impact energy compared to that on crystalline ice target. Therefore, the crater diameter on the porous mixture is smaller than that on the crystalline ice at high impact energy (>100 J), but larger at low impact energy (<100 J).

Recently, numerical simulations have been applied to asteroid collisions in addition to laboratory experiments (Asphaug *et al.* 1998, Nolan *et al.* 2001). In asteroid collisions, self-gravity is the most important attraction force against the impact and controls the impact strength of small asteroids. To simulate the collision of rubble pile bodies having self-gravity, numerical simulation seems to be the best method. Asphaug *et al.* (1998) showed that the impact damage was quite limited just below the impact site in a porous small asteroid because the shock wave decayed very quickly with propagation. Although numerical simulation is a very powerful method of including a gravity effect on planetary cratering and disruption, the result of this method is highly dependent on the adopted equation of state, theory of fracturing, and related material parameters. So, laboratory experiments to study the elementary processes of impact cratering and disruption are necessary not only for the perfectly compacted or crystalline materials but also for the porous materials.

Love *et al.* (1993) studied porosity effects on impact cratering and disruption. They performed eight hypervelocity (4.9–6.0 km/s) shots onto porous (porosity $\phi = 5, 37, 39$, and 60%) sintered aggregate glass targets. These targets were prepared by temperature-driven sintering. The only pressure used to sinter their targets was the targets' own weight. Love *et al.* (1993) found that the impact strength increases with increases in target porosity (ϕ) and it is proportional to $(1 - \phi)^{-3.6}$. The increase of the impact strength in a porous target has been also recognized in gypsum and clay targets (Davis and Ryan 1990). Ryan *et al.* (1999) also studied the impact properties of a porous ice target as a simulated material of Kuiper Belt objects (KBO). They found the same effect of porosity on the strength.

There seem to be many porous icy bodies in the outer Solar System in addition to KBO: icy satellites and comets. Water ice is a very common material in the outer Solar System that constructs satellites and comets. The impact properties of ice have been studied in relation to the collisional evolution of icy bodies (Arakawa *et al.* 1995, 2000, Arakawa 1999a, 1999b, Arakawa and Higa 1996, Kato *et al.* 1995, Lange and Ahrens 1987, Kawakami *et al.* 1983). Thus, the impact strength of ice and other physical properties of ice related to the fundamental processes of impact disruption were clarified to advance the discussion of the collisional accretion. However, the previous studies on the water ice are not enough to research real icy plan-

ets because the icy planets are composed of not only ice but also silicates. Lange and Ahrens (1983) examined the tensile strength of an ice–rock mixture (5 ~ 30 wt% in rock) in low-velocity impact and determined that the strength of the mixture was about 30% stronger than that of pure water ice.

Small icy bodies are considered to have large porosities in their interiors as small silicate bodies. There are several icy satellites with densities near or lower than 1000 kg/m^3 ; also, the density of comet nuclei is estimated to be less than 1000 kg/m^3 (Rickman 1998). Leliwa-Kopystynski and Kossacki (2000) calculated the evolution of the internal structure of small icy bodies composed of icy-silicate porous mixture. They showed that the porosity decreased from its initial state by temperature- and pressure-driven rheological processes. Thus, we think that primitive small bodies should have large porosities. The porosity could be changed according to the stage of the thermal evolution driven by heat conduction and heat production in the processes of decay of radioactive elements and of gravitational self-compaction. It is therefore reasonable to study the different properties of the porous icy-rocky mixtures. In particular it is worth simulating the collisional evolution of icy bodies.

In this paper, we present our experimental results of high-velocity impacts onto porous, well-sintered icy-silicate cylindrical blocks. The porosity dependence of impact strength and the effect of silicate contents on the strength of ice–silicate mixtures are described in detail. High-speed images are taken to observe ejecta excavated from the crater. As a result, accretion and disruption conditions in the collision of icy bodies and their implications for the planetary formation process are discussed.

2. EXPERIMENTAL METHOD

2.1. Sample Preparation

Two types of samples were prepared with natural snow and silicate (pyrophyllite) powder. One is a pure water ice target and the other is a mixture target of ice particles and silicate powder. A full list of the samples is given in Table I.

For the pure ice target, four different porosities (0, 10, 24, 37%) were prepared by pressure sintering of snow. Natural snow with the average grain size of $\sim 100 \mu\text{m}$ was compressed to required porosity at -10°C . The snow was put into a stainless-steel cylinder with a diameter of 10 cm and compressed by a piston at constant displacement speed of $8 \times 10^{-4} \text{ mm/s}$. The pressure was applied for a period from one-half to several hours, depending on the requirement for final porosity. The maximum pressure of 3 MPa was applied to the snow during the sintering. It was expected that there would be residual stress in the sample after it was recovered from the cylinder. Therefore, the recovered sample was stored in a cold room (-18°C) for 2 months to relax the internal stress as well as to undergo the further, temperature-driven sintering (for the mechanisms of sintering, see, e.g., Eluszkiewicz *et al.* 1998). To obtain the highest porosity of 55%, we used a natural sintered snow collected at Nakayama

TABLE I
Experimental Conditions and Results

Run No.	ρ (g/cm ³)	M_t (g)	V_i (m/s)	m_1 (g)	m_1/M_t	Q (J/kg)	$f_{0.5}$	V_{e-max} (m/s)	θ^a (°)	Misc.
Pure water ice target										
Porosity = 55%										
517-1	0.392	307.8	303	75.3	0.245	235	0.14	44.6	n.d.	
517-2	0.402	315.7	203	316.5	1.003	104	n.d.	39.0	36.8	Comp.
518-1	0.397	312.0	157	313.3	1.004	63.3	n.d.	27.8	27.9	Comp.
518-2	0.402	315.9	455	63.4	0.201	528	0.06	49.7	27.4	
518-3	0.356	279.7	545	35.3	0.126	850	0.06	41.3	37.5	
518-4	0.400	313.7	645	62.3	0.198	1061	0.021	87.7	49.4	
Porosity = 37%										
521-1	0.576	452.3	294	259.4	0.574	153	0.15	154	35.9	
521-2	0.578	453.6	216	391.2	0.862	82.3	0.3	84.4	50.1	
521-3	0.578	454.2	455	46.7	0.103	365	0.038	194	51.6	
521-4	0.573	450.1	561	79.5	0.177	559	0.043	278	53.1	
521-5	0.575	451.3	652	62.3	0.138	754	0.02	344	54.1	
521-6	0.578	454.2	152	391.5	0.862	40.7	0.37	72.5	30.6	
Porosity = 24%										
521-7	0.700	549.4	305	166.4	0.303	135	0.06	195	43.1	
521-8	0.683	536.3	216	406.0	0.757	69.6	0.27	179	32.2	
522-1	0.692	543.1	457	88.2	0.162	308	0.025	310	50.2	
522-2	0.690	542.0	560	71.1	0.131	463	0.012	385	51.5	
522-3	0.698	548.1	647	55.6	0.101	611	0.0027	444	59.0	
522-4	0.690	542.0	161	446.7	0.824	38.3	0.32	110	35.4	
Porosity = 10%										
523-1	0.807	633.8	277	447.9	0.707	97.4	0.09	290	45.3	
523-2	0.828	650.2	218	321.1	0.494	58.5	0.04	316	32.3	
523-3	0.817	642.0	462	17.7	0.0275	267	0.001	452	47.1	
523-4	0.824	647.4	568	18.2	0.0280	399	0.0014	626	49.2	
523-5	0.820	644.1	663	15.2	0.0235	547	0.0004	656	57.6	
523-6	0.793	622.4	163	154.1	0.248	34.2	0.14	187	32.1	
Porosity = 0%										
611-6	0.908	584.0	303	75.3	0.129	126	0.015	395	43.7	
611-7	0.889	696.3	441	18.2	0.0261	223	0.0011	550	48.7	
Mixture target										
Porosity = 38%										
523-7	0.836	656.9	153	652.3	0.993	28.5	n.d.	56.8	38.9	Crater
523-8	0.835	655.6	227	499.2	0.762	63.0	0.2	110	36.3	
524-1	0.832	653.7	288	372.1	0.569	102	0.07	141	32.4	
524-2	0.836	656.4	423	210.5	0.321	218	0.021	160	39.2	
524-3	0.838	658.5	556	133.2	0.202	376	0.008	328	50.8	
524-4	0.833	654.3	667	77.5	0.119	544	0.0043	320	42.9	
Porosity = 0–39%										
611-1	0.988	272.6	221	186.8	0.685	143	0.1	115	39.8	26%
611-2	1.204	322.8	221	250.5	0.776	121	0.27	228	21.6	13%
611-3	1.316	323.6	214	297.0	0.918	113	0.4	849	0	0%
611-5	0.845	228.0	214	114.8	0.504	161	0.03	102	29.5	39%

^a Ejecta angle θ is defined in Fig. 5. The column named Misc. contains miscellaneous information related to the experiment. “Comp.” means that the projectile was captured in the target by the compaction of the porous sample. “Crater” means that the target was not disrupted but the impacted region was excavated. Porosity of the last four samples is listed in the Misc. column.

mountain pass in the winter of 2001. The naturally sintered snow block, which was homogeneous without layered structures, was cut into the cylinders. All pure icy targets were cylindrical with a diameter of 10 cm and a height of 10 cm.

The mixture target was prepared by mixing ice particles (natural snow) with silicate powder (pyrophyllite). Since several impact results for pyrophyllite are reported (Takagi *et al.* 1984), and in addition pyrophyllite can be crumbled into powder very easily, we chose this material for our silicate sample. The size of the pyrophyllite powder grains was less than $\sim 10\ \mu\text{m}$. The mixed mass ratio of snow and pyrophyllite was 1 : 1. Two sets of different size targets were made by means of the sintering method described above. They are cylindrical in shape with a diameter of 7 cm and a height of 7 cm or with a diameter of

10 cm and a height of 10 cm. For the six 10-cm targets, only one porosity of 38% was made. The four different porosities (0, 13, 26, 39%) were prepared for 7-cm targets. The icy-pyrophyllite targets were stacked in a cold room at -18°C together with the pure ice samples.

2.2. Impact Experiments

Impact experiments were conducted at the Institute of Low Temperature Science, Hokkaido University. All experiments were carried out in a large cold room at a temperature of -10°C . One-stage light gas gun (vertical type) installed in the cold room was used to accelerate the projectile made of water ice. This icy projectile was a cylinder with a diameter of 15 mm, a height of 10 mm, and a mass of 1.6 g. The projectile was launched in the direction normal to the top flat plane of the cylindrical target and the impact occurred at the center of the flat surface. Our results should be applied only for central impact, i.e., where the impact angle, measured from the local vertical, is zero degree. Since most impacts in the Solar System are not central, modelers should be aware of this constraint. The impact velocity was from 150 to 670 m/s. The detailed description of the impact method was presented in Arakawa *et al.* (1995).

The target was set in 30-cm acrylic cubic box assigned to recover the impact-produced fragments (Fig. 1). There was a hole, 3 cm in diameter, in the center of the top cover of the box, to allow free passage of the projectile. To minimize disruptions

of the fragments by means of their collisions with the walls of the acrylic box, we installed soft and thick sponge plates on one pair of the opposite sides of the box and on its bottom. However, since one pair of the sides should be used as an optical window to take the high-speed pictures, we did not cover these sides with sponges. There may be a small effect of secondary impacts on the size distribution of the fragments, especially for high-porosity targets, since they are very fragile. The acrylic box was set in a target chamber, and the chamber was evacuated to about 1000 Pa before the shot. After the shot, the impacted target was recovered from the box, and each fragment was weighted with an electric balance in the cold room. The individual fragments with mass larger than about 0.12 g were counted to construct the function of mass distribution. The smallest fragments and the recovered dust were weighed altogether to check the completeness of the recovery.

2.3. High-Speed Camera Observation

Impact ejecta excavated from a growing crater was directly observed by using an image-converter camera (Fig. 1). To enhance ejecta curtain composed of tiny dust, we used a shadow photograph lighting system like that used by Arakawa (1999a). A Xe-flash lamp was a light source of this system with two concave mirrors (each mirror size is 15 cm). The lamp has a strong brightness (>50 J per one flash) and flash duration longer than 1 ms. That was sufficient for the camera to record a series of the images of the disruption process. The image-converter camera (Ultra NAC, Japan) can take up to 24 successive images in one run. Each interval between the consecutive frames can be adjusted. We have changed the intervals from $10\ \mu\text{s}$ (during the beginning of the event) to $100\ \mu\text{s}$ (at the end) for each record. This corresponds to 10^5 – 10^4 frames per s. A laser beam and a photodiode were set just above the target surface to detect the projectile going through and were used for the trigger to work the image-converter camera. The same method was used to measure the launching velocity of the ice projectile. This speed meter was set just below the launch tube, close to the acrylic box containing the target.

3. EXPERIMENTAL RESULTS

3.1. Observation of Cratering Ejecta

For each impact experiment, the image-converter camera has taken sets of 12 photos on one individual frame (Figs. 2a and 2b). A black shadow on each photo shows the envelope of expanding ejecta. The first image on each frame is at the moment of impact. After contact of the projectile onto the target surface, the projectile can be observed to penetrate into the target with time. The images on one individual frame are for the time intervals 10, 10, 10, 10, 10, 10, 40, 40, 40, 100, and $100\ \mu\text{s}$. They correspond to the time intervals from the moment of impact equal to 0, 10, 20, 30, 40, 50, 60, 100, 140, 180, 280, and $380\ \mu\text{s}$. (Images of the runs 517-1, 517-2, and 518-2 are exceptions; however, time intervals for them were 0, 5, 10, 15, 20, 25, 30, 50, 70, 90, 140, and

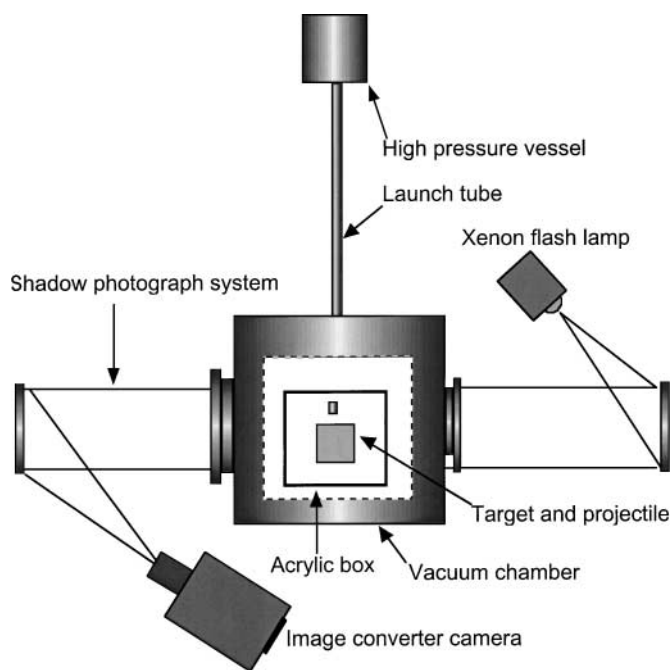


FIG. 1. Scheme of the experimental setup and of the observation system with the image-converter camera. The vertical type of He-gas gun is installed in a cold room. The target placed in the acrylic recovery box is set in the vacuum chamber. The shadow photograph lighting system is used to observe the high-speed ejecta.

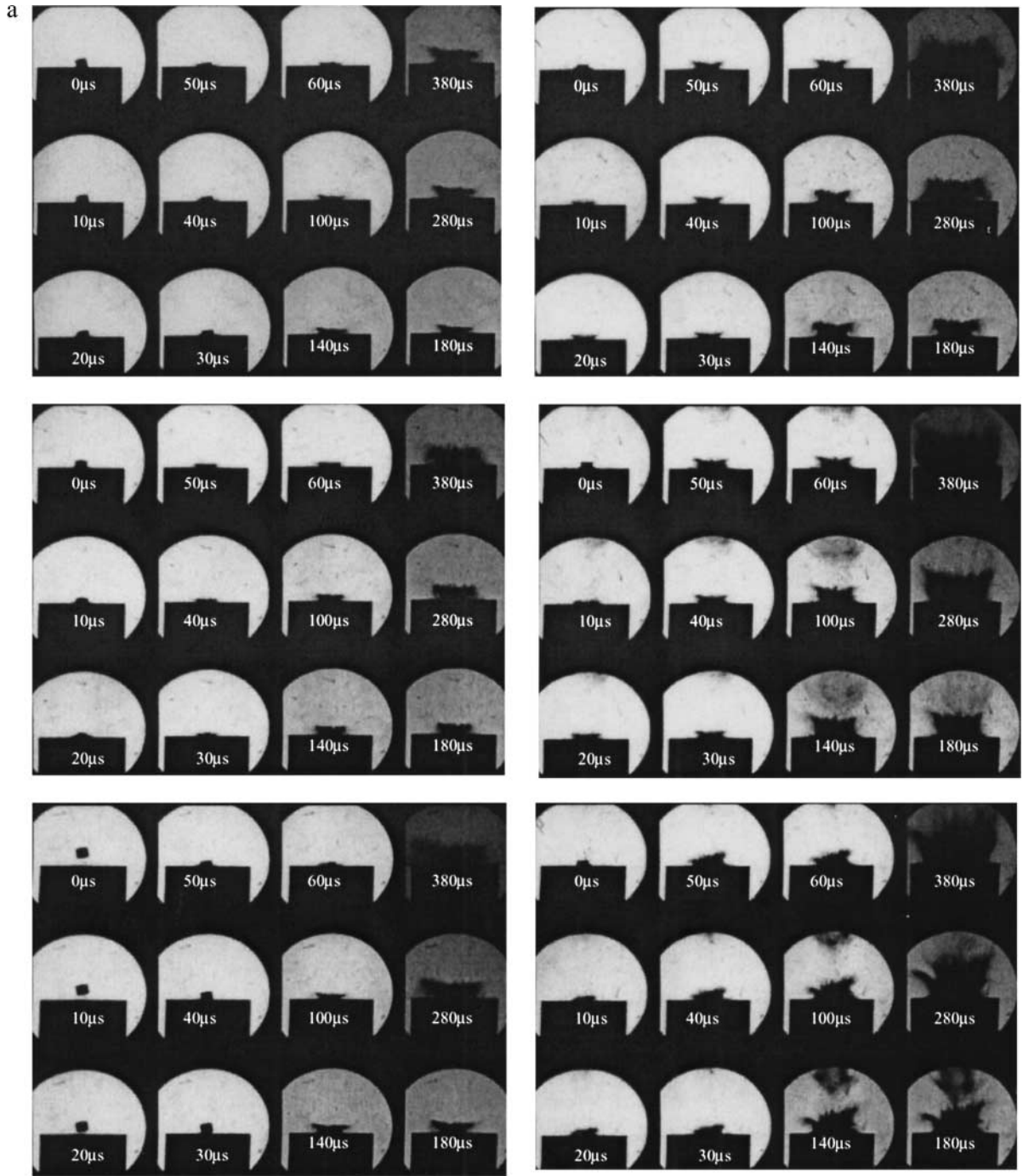


FIG. 2. (a) The matrix of six frames corresponding to fixed composition (ice only, $C = 0$) and fixed porosity ($\phi = 0.37$). Impact velocity V_i is a parameter. The consecutive frames are for the following runs: 521-6, $V_i = 152$ m/s; 521-2, $V_i = 216$ m/s; 521-1, $V_i = 294$ m/s; 521-3, $V_i = 455$ m/s; 521-4, $V_i = 561$ m/s; 521-5, $V_i = 652$ m/s. We can observe formation of ejecta plums with time. For larger impact velocity, ejecta move faster and they are more intensive. (b) The matrix of four frames. Impact velocity $V_i \approx 217$ m/s. Left column, $C = 0$, runs: 523-2, $\phi = 0.1$; 521-2, $\phi = 0.37$; right column, $C = 0.5$, runs: 611-2, $\phi = 0.13$; 611-5, $\phi = 0.39$.

180 μ s.) The consecutive photos are from the top leftmost, down the first column, up the second column, down the third column, and up the fourth column to the uppermost right. Regarding the individual photos, we can estimate that an error of the zero point

of time scale is not larger than 10 μ s. The endmost frame, top right, 380 μ s after an impact, corresponds to the situation before the disruption (if any) of the target: A rectangular shadow of a cylindrical target is still visibly intact on the sides.

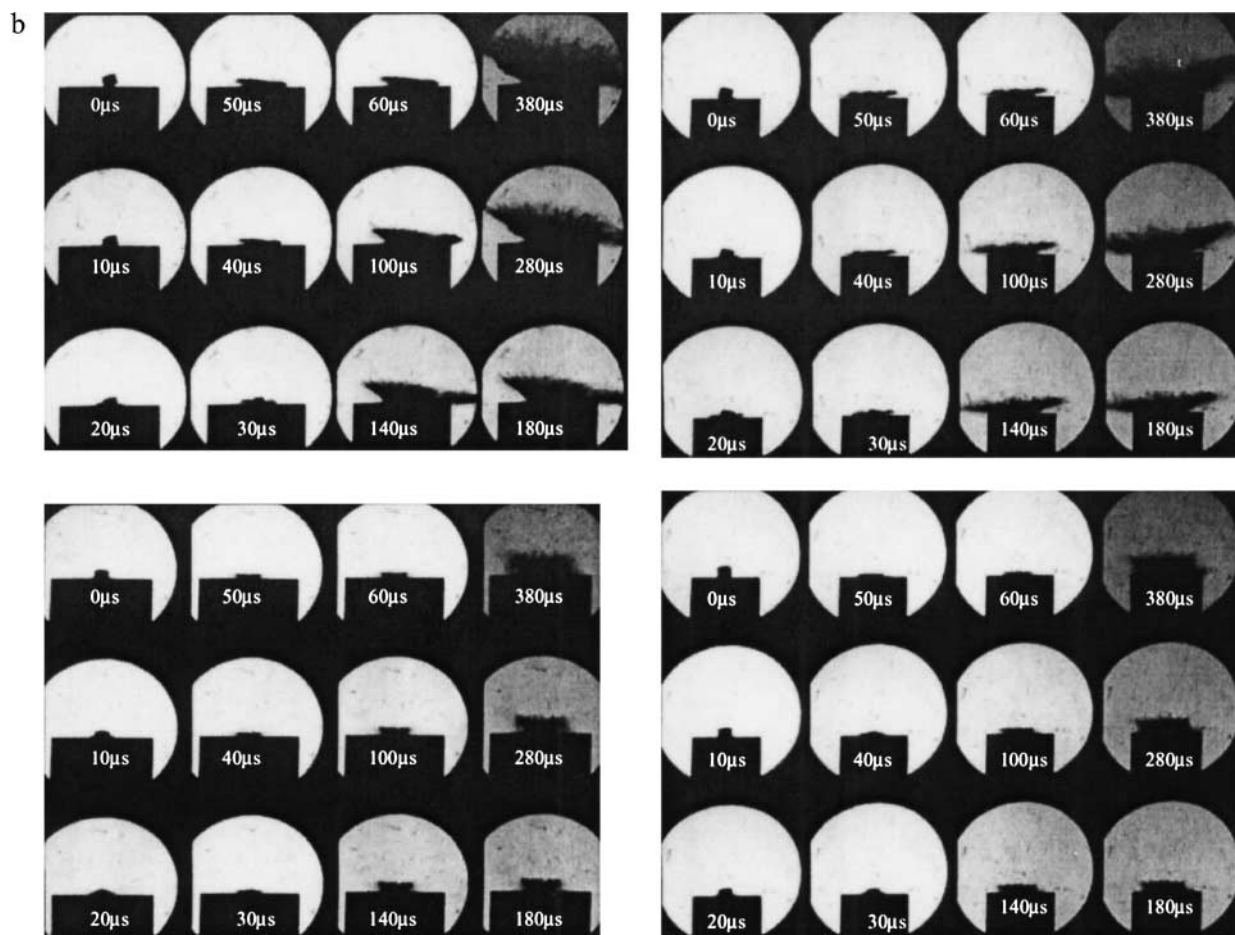


FIG. 2—Continued

The frames, each of 12 photos, can be properly arranged to form a “matrix.” The simple matrix corresponds to the constant values of all but one parameter. A matrix of this type that can be built up from our experimental material contains up to six frames. An example is given in Fig. 2a. The impact velocity is the only parameter to change from 152 to 652 m/s. We note that the ejecta plume expands at higher velocity with the increase of the impact velocity. Another type of matrix is given in Fig. 2b: The frames for four different shots form a matrix of 2×2 . This matrix allows comparison of an influence of changes of porosity (vertical columns) and changes of composition (horizontal rows) onto formation of the ejecta plumes. For the targets with low porosity, the ejecta plumes are considerably different from those for highly porous targets. However, the composition factor C does not strongly influence the ejecta pattern.

We will compare the ejecta formation, ejecta velocity, and disruption process for two very different targets impacted with very different velocities. So, we consider the run 517-2 (pure icy target with porosity 55%, impact velocity 203 m/s) and the run 524-4 (icy-pyrophyllite target with porosity 38%, impact velocity 667 m/s). For other details of the runs, see Table I. Figure 3a shows the observed successive images taken by the

image-converter camera for run 517-2. The black shadow shows the target and the envelope of expanding ejecta. The first image of Fig. 3a is at the moment of impact. After contact of the projectile onto the target surface, the projectile can be observed to penetrate into the target with time. A small amount of ejecta was excavated from the edge of the penetrating projectile, but the ejecta velocity looks very slow relative to the impact velocity: the maximum ejecta velocity was less than 20% of the projectile velocity. The target was not broken by this impact and it was recovered almost intact (Fig. 4a). In addition, the mass of the recovered target increased about 0.8 g: this means that the projectile was captured in the target completely and the ejected material from the crater was less than 0.8 g. Figure 3b shows the successive images for run 524-4. The high-speed ejecta can be observed in these images and the envelope of expanding ejecta shows an inverse cone shape as is usually observed in impact cratering on sand. The angle between the target impact surface and the inverse cone formed by the ejecta envelope is about 43° . The maximum velocity of the ejecta was observed on the edge of the inverse cone to be about 48% of the projectile velocity. The target was completely disrupted into small fragments as shown in Fig. 4b.

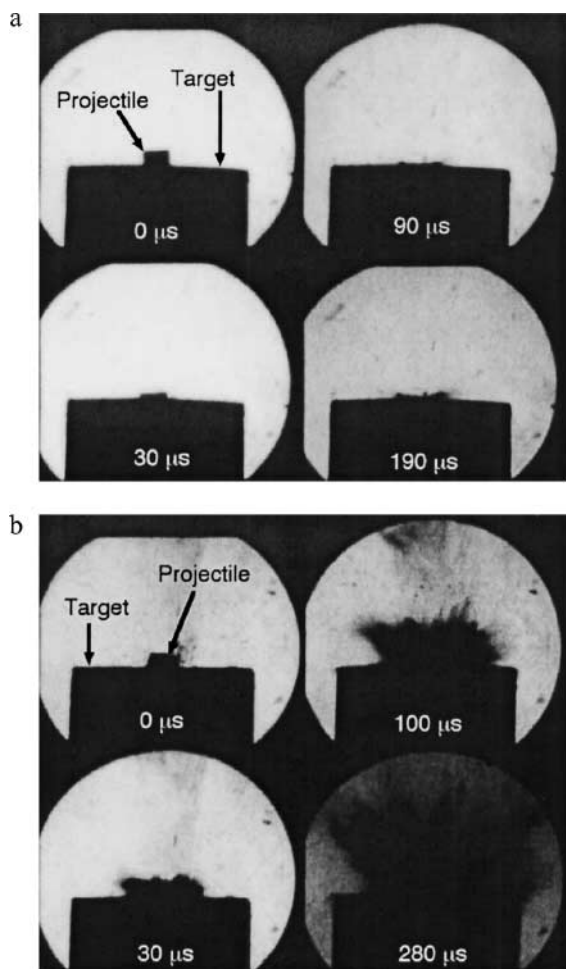


FIG. 3. The successive images taken by the image converter camera. (a) Run 517-2. (b) Run 524-4. The black shadows in the center of a white circle are a target and a projectile. Four images are selected from 12 successive images in one shot. The time after the moment of impact for each image is shown in μs .

Figure 5 shows contours of the ejecta envelopes at each time after the impact for run 524-4. The first six contours are shown at every $10 \mu\text{s}$, and then the contours are drawn at 90, 130, 170, and $270 \mu\text{s}$. To analyze the ejecta flow, we define the ejecta angle (θ) as shown in this figure. The θ is an angle between the target surface and the direction of the ejecta with the maximum velocity 43° in this case. Figure 5b also shows the contours at the impact velocity of 441 m/s for less porous (3%) pure ice, run 611-7. The ejecta angle is almost the same as that of run 524-4, but the maximum ejecta velocity was observed to be more than 120% of the impact velocity.

The ejecta angle was analyzed for every shot and summarized in Fig. 6a against the impact velocity. The measured ejecta angle at the low-impact velocity around 200 m/s is in the range from 30° to 40° , irrespective of the target types. The ejecta angle almost linearly increases up to 60° with the increase of the impact velocity from 200 to 700 m/s, but a few data of pure ice target with 55% porosity are out of this trend (they are slightly lower).

We notice that the ejecta angle depends only on the impact velocity, irrespective of the porosity and the silicate contents.

Figure 6b shows the maximum ejecta velocity normalized by the impact velocity ($V_{e-\text{max}}/V_i$) vs the impact velocity for each type of target. The maximum ejecta velocity is almost constant irrespective of the impact velocity. This normalized velocity increases with decreasing target porosity. When we compare $V_{e-\text{max}}/V_i$ of pure ice target with 37% porosity to that of mixture target with the same porosity, it is impressive that their $V_{e-\text{max}}/V_i$ are almost similar to each other, in spite of the apparent difference in the composition (silicate contents). Other data of mixture targets with various porosities are also similar to those of pure ice having the same porosity. Then, the relationship between the target porosity and the $V_{e-\text{max}}/V_i$ was analyzed in Fig. 7. The

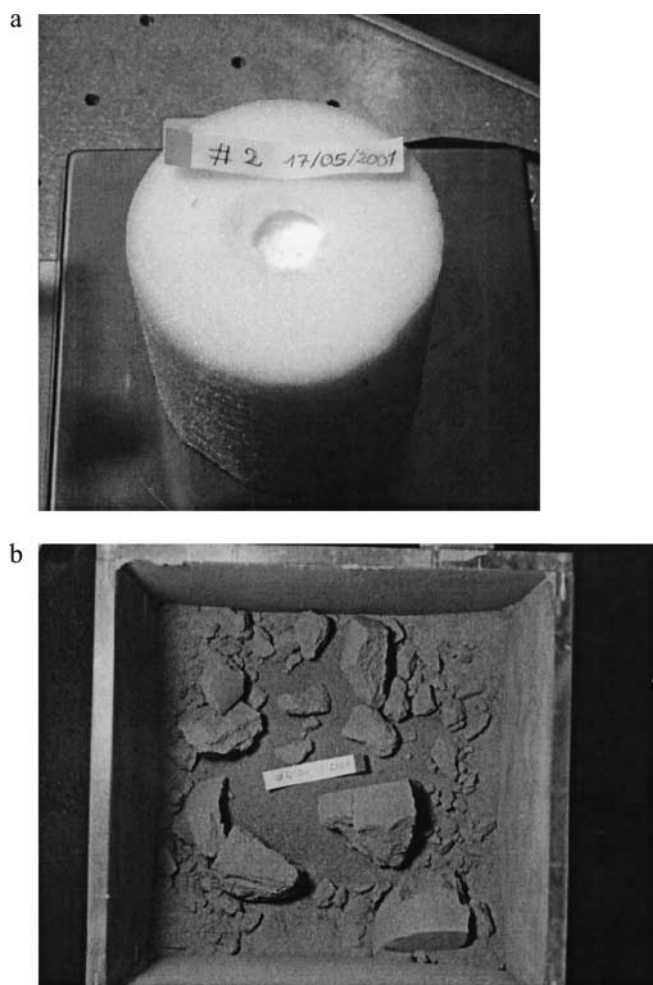


FIG. 4. Photographs of recovered target after impact. (a) Run 517-2. The target did not break at all. The mass of the target after recovery increased 0.8 g because of the capture of the projectile. There is a hole in the center of the impact surface. Its diameter is almost the same as the projectile diameter. This hole is formed by the impact-generated compaction of the porous target. (b) Run 524-4. This photo was taken just after the impact, so we see that all of the fragments were in the recovery box. The target is completely disrupted and there are several large fragments and several tens of small fragments. More than 30% of the mass was disrupted into fine particles and they are accumulated at each of the four corners.

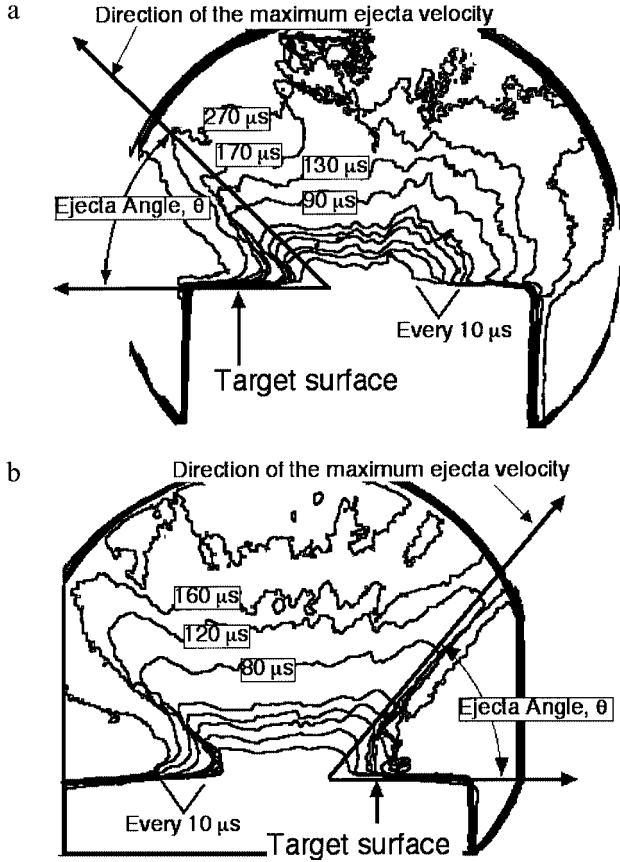


FIG. 5. Contours of ejecta envelope reconstructed from the images of the high-speed camera. (a) Run 524-4. (b) Run 611-7. First four or five contours are shown every 10 μs . After 80 or 90 μs , the time after the impact is shown on the contour line. The maximum ejecta velocity and the ejecta angle are obtained from these figures. The ejecta angle is defined as the angle between the target surface and the direction of the maximum ejecta velocity.

averaged $V_{e-\text{max}}/V_i$ at each porosity for two types of targets, pure ice and mixture, is depicted by closed and open square symbols, respectively. These data seem to lie on one line, irrespective of the silicate contents. Then, the data are fit by the simple linear equation in the porosity range from 0 to 0.6 altogether. The derived empirical equation is

$$V_{e-\text{max}}/V_i = -(2.17 \pm 0.13)\phi + (1.29 \pm 0.04), \quad (1)$$

where the correlation coefficient of this fitting is 0.97. It is noted that the maximum ejecta velocity strongly depends on the porosity and it linearly decreases from 1.3 to 0.1 when porosity increases from 0 to 0.55. The ejecta velocity higher than the impact velocity was observed in the target with the porosity lower than 15%. Such high-velocity ejecta were also observed in Arakawa and Higa (1996) and Arakawa (1999b) in ice-on-ice impact. They suggested that the jetting mechanism could work to accelerate the ejecta to achieve a velocity higher than the impact velocity. Then, it would be reasonable to think that the jetting mechanism caused the high-velocity ejecta in our case when the

target porosity was not so high (less than 15%). We can imagine that almost no ejecta will come out of the crater if an impact occurs onto a target with porosity higher than 60%. Although the obtained relationship between the porosity and the maximum ejecta velocity is quite clear and simple, the mechanism that causes this relationship seems to be complex. According to the simple cratering model, e.g., D. E. Maxwell's Z-model (Melosh 1989), the ejecta velocity can be determined by the geometry of the propagating shock wave and the decay of the particle velocity in the target. Unfortunately, we do not have enough knowledge about these factors for porous icy and icy-mineral targets to discuss the physical background of Eq. (1). In our future work, we will clarify the mechanism and explain Eq. (1).

3.2. Mass Distribution of Impact Fragments

The largest fragment mass normalized by the original target mass, m_l/M_t (see Table I), is the most typical parameter to

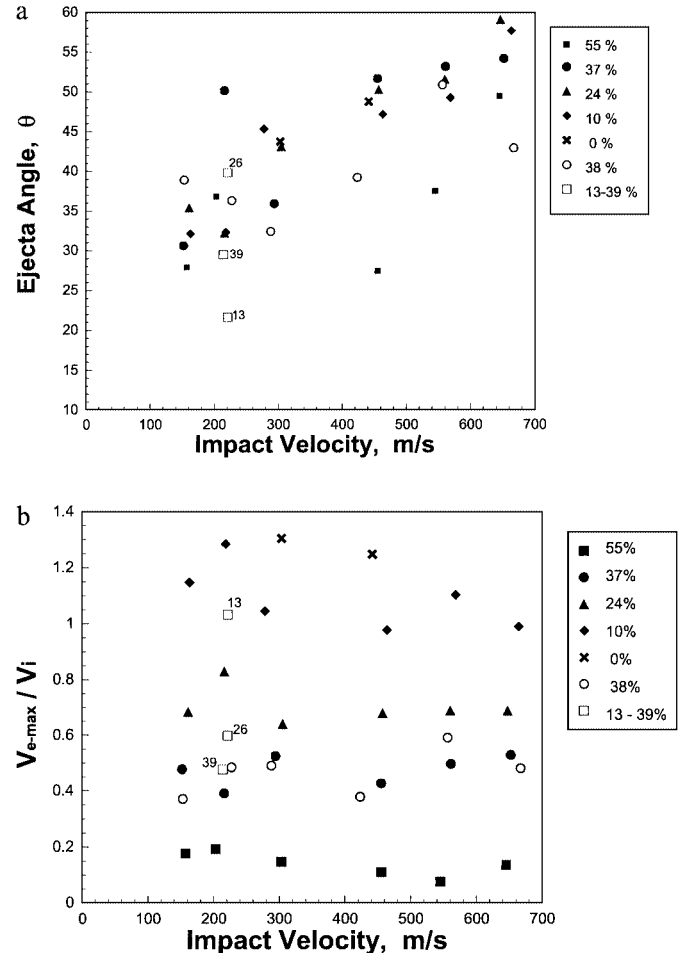


FIG. 6. (a) Ejecta angle vs impact velocity observed in the high-speed images. (b) The maximum ejecta velocity normalized by the impact velocity vs impact velocity. Closed symbols mean pure ice targets, and open symbols mean icy/mineral targets. The open squares mean the targets with various porosities, then the porosity is noted in the figure as the number in percent.

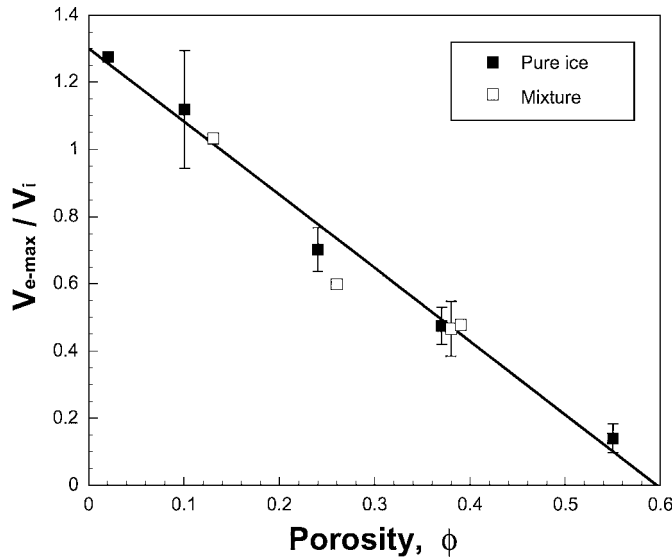


FIG. 7. Porosity dependence of the maximum ejecta velocity normalized by the impact velocity in pure ice and in mixture target. Each data point is the average of the data at different velocities in Fig. 6b. The error bar is the standard deviation coming from this averaging. There is no apparent difference among pure ice and mixture data, then the least-squares fit was conducted for all of the data and the result is drawn on the figure as a straight line.

describe the degree of impact disruption of the target. Energy density (Q , see Table I), defined as a projectile kinetic energy divided by a target mass, is a scaling parameter used in many impact experiments to describe the impact condition related to the impact disruption. Therefore, at first we study the relationship between these two parameters in our two types of targets. Figure 8

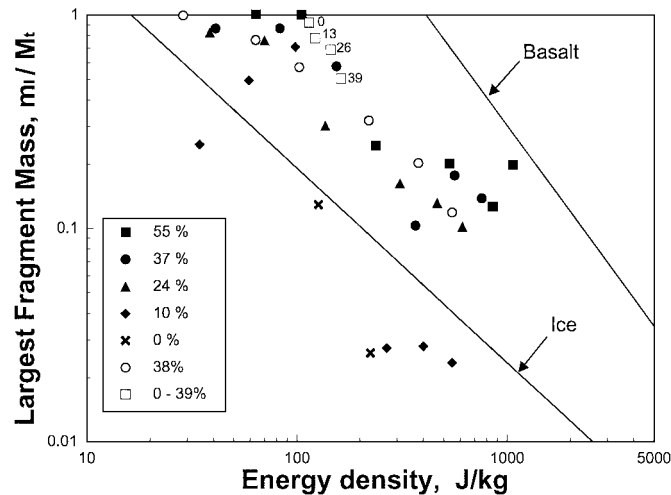


FIG. 8. Energy density vs largest fragment mass for two types of target (pure ice and mixture). Closed symbols mean pure ice targets, and open symbols mean icy/mineral targets. The open squares mean the targets with various porosities. Then the porosity is noted in the figure as the number in percent. There are two straight lines for the comparison with our data: The line for pure and nonporous icy targets that comes from Arakawa (1999a) and the line for basalt that comes from Fujiwara *et al.* (1977).

shows the relationship between the largest fragment mass normalized by the original target mass (m_i/M_t) and the energy density (Q). The data with different porosities are shown by different symbols. We can find that m_i/M_t for low-porosity targets (0%, 10%) is clearly lower than that for high-porosity targets (24, 37, and 55%) at a constant energy density, although the data of each porosity and each type of target scatter very much. Moreover, it could be found that m_i/M_t for pure icy target with porosity 24% is slightly lower than that for the targets with higher porosity. The data for 0 and 10% porosity targets and the data for 37 and 55% porosity targets are well mixed in this figure, so we cannot see any differences depending on the porosity between them. The results for the mixture target with 38% porosity are mixed with the data for pure icy targets with porosities of 37 and 55%. The ratio m_i/M_t for the mixture targets with different porosities is also among the results for high-porosity targets in pure ice. However, they obviously show a trend to increase with the decrease in porosity: the non-porous mixture target shows the largest m_i/M_t value in a whole group of the mixture targets.

The shattering critical specific energy (Q_s^*) is usually used in laboratory results to describe impact strength and is defined as Q value at the $m_i/M_t = 0.5$ (Melosh and Ryan 1997). The impact strength for low-porous (0%, 10%), pure icy targets is roughly derived (see Fig. 8) to be 40 J/kg according to the following result of the data fitting: $m_i/M_t = 10^{1.73 \pm 0.73} Q^{-1.27 \pm 0.33}$. That for high-porous (37%, 55%), pure icy targets is about 134 J/kg according to the following result of the data fitting: $m_i/M_t = 10^{1.23 \pm 0.27} Q^{-0.72 \pm 0.11}$. This means that there is a clear dependence of the impact strength on the target porosity: the impact strength increases with increases in target porosity. The impact strength of the mixture target with the porosity 38% is well determined to be 99 J/kg according to the following result of the data fitting: $m_i/M_t = 10^{1.13 \pm 0.16} Q^{-0.72 \pm 0.07}$; the data of m_i/M_t are well organized to become a straight line in Fig. 8. The previous data for water ice and basalt are also plotted in Fig. 8. The results for our porous targets are between the basalt and ice line. Unfortunately, the measured m_i/M_t scatters too much to us to have a detailed discussion of the porosity dependence on the impact strength.

3.2.1. Pure Ice

Figure 9 shows size distributions of the impact fragments for pure icy targets with a porosity of 37%. The size distributions are shown in the form of a cumulative number of the fragments vs fragment mass normalized by the original target mass (m/M_t). Impact velocity is a parameter. It is obvious that the mass of the largest fragment decreases with increases in impact velocity. So, the first point (the rightmost point of the distribution) for higher velocity impact is on the left side of that for lower velocity impact. Each distribution in the small fragment region shows a power-law relationship, approximately. The slopes of each distribution are almost the same, 0.6, irrespective of the impact velocity. The cumulative number corresponding to the left-hand side of the distribution ($m/M_t \approx 0.0002$) differs by one order

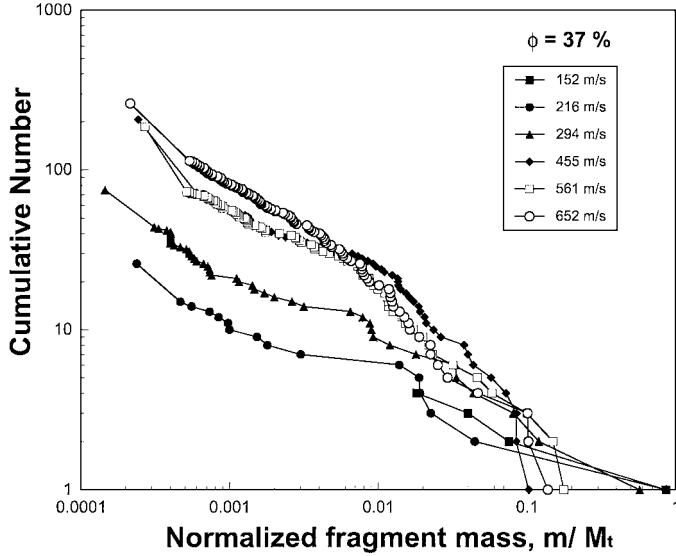


FIG. 9. Size distribution of the impact fragments recovered from the pure icy target with the porosity 37% impacted at different velocities. The distribution is presented as the relationship between the cumulative number of the fragments and the normalized fragment mass.

of magnitude between the result for 216 m/s impact and the result for 652 m/s impact. The same trend is observed for the icy targets with porosity lower than 37%. However, the distributions for 55% porosity target are different. Systematic changes in the size distribution depending on the impact velocity have been observed in ice-on-ice impact (Arakawa *et al.* 1999a, Kato *et al.* 1995). Therefore, it would be reasonable to expect that the general properties of the size distribution can be applied to porous icy targets with porosity less than 37%.

We can express the size distribution differently from that shown in Fig. 9. Figures 10a and 10b (for the icy targets with porosities of 37 and 55%, respectively) use cumulative mass of the fragments normalized by the original target mass. This distribution increases toward the right-hand side. The slopes of the distributions at the smaller mass region show the power-law relationship of each distribution. This character is essentially identical to that found in Fig. 9 at a small fragment mass region. It is interesting that the distributions presented in Fig. 10b do not have power-law relationships in the small fragment region. Instead, the cumulative mass is almost a constant value for the impacts of 545 and 645 m/s, and it remains nearly a constant until the normalized fragment mass becomes larger than 0.01. The target with the porosity of 55% is quite fragile because the cohesion among ice particles is very weak: the static compressive strength of snow with the porosity of 55% is about two orders of magnitude weaker than that of crystalline ice (Mellor 1975). Then, the sintered snow target easily separates into ice particles only by weak compressive stress. Therefore, after the collision, many separated ice particles were recovered with several large fragments. This special character of the target, that the cumulative mass is a constant in the range of the small fragment

mass, means that the fragments smaller than some critical size easily separate. However, we cannot neglect the effect of a secondary impact for the recovered fragments. Because of the weak strength, the porous fragments can easily disrupt into ice particles by the secondary impacts on the walls of the recovery box even if we set sponge plates on the sides.

As we mentioned in the previous section, the masses of the largest fragments of the impacted porous targets are so scattered (see Fig. 8) that a detailed discussion of the porosity dependence

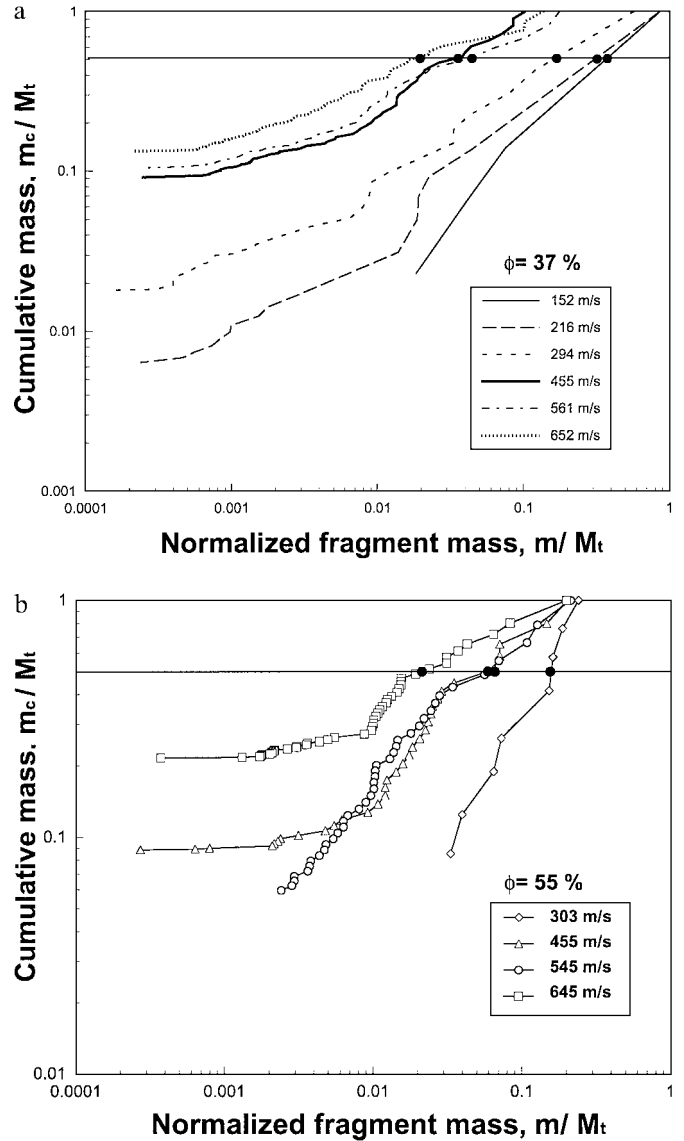


FIG. 10. Size distribution of the impact fragments shown by the relationship between the cumulative mass and the normalized fragments mass. (a) The distributions are for pure ice target with the porosity of 37%. The reference line of $m_c/M_t = 0.5$ is drawn and the cross points with each distribution are shown by the symbols of closed circle. We use the normalized fragment mass at these cross points instead of the largest fragment mass to represent the degree of disruption. (b) The distributions are for pure ice target with the porosity of 55%.

on the impact strength is impossible. We found that the normalized fragment mass at the cumulative mass of 0.5 had a quite good correlation with the degree of impact disruption shown by the size distribution, and, moreover, it sometimes had a better correlation with energy density. For example, the size distributions in Fig. 10a are arranged in the order of the impact velocity: the lowest distribution corresponds to the result of 152 m/s and the uppermost distribution corresponds to the result of 652 m/s. This order is strictly kept just before the cumulative mass is less than 0.6. However, for the impact of 455 m/s, the cumulative mass abruptly increases in the region of the cumulative mass above 0.5. As a result, the order of the largest fragments does not follow the order of the impact velocities. If we use the fragment mass at $m_c/M_t = 0.5$ instead of the largest fragment mass, this inconsistency can be avoided. The largest fragment may be often formed by the accidental stochastic process. Then, for giving more physical information included in the size distribution, we recommended using the normalized fragment mass corresponding to cumulative mass $m_c/M_t = 0.5$ instead of the largest fragment mass. We denote hereafter this particular normalized fragment mass as $f_{0.5}$.

Figure 11 shows the relationship between the normalized fragment mass $f_{0.5}$ and the energy density Q . Results for the sets of targets with the same porosity are clearly separated. They can be fitted by the power-law equation as follows:

$$f_{0.5} = q_0 Q^p. \quad (2)$$

The constants q_0 and p for each porosity are shown in Table II. We introduce a new parameter, $Q_{0.5}^*$, closely related to the impact strength according to the obtained relationships shown in Eq. (2).

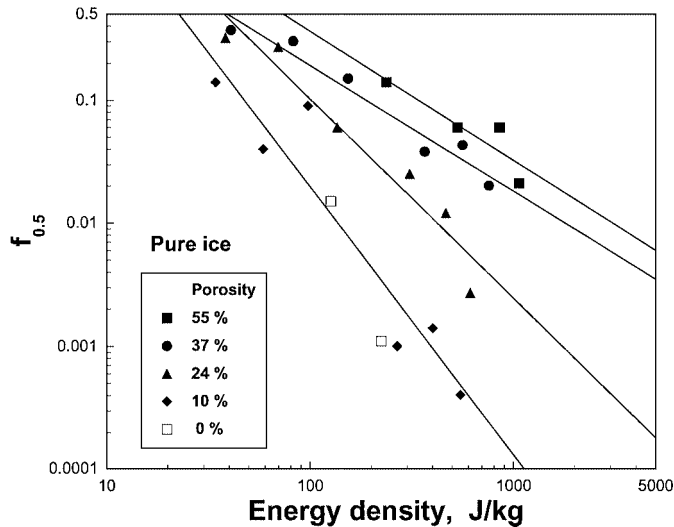


FIG. 11. The relationship between $f_{0.5}$ and energy density for pure icy target. Each line is calculated by least-squares fitting for each porosity data. Two points denoted “0%” are for the densities 908 and 889 kg/m³, therefore for the porosities of 1 and 3%, respectively. These points are just included for comparison but not fitting the line for 10% porosity.

TABLE II
Calculated Parameters in Eq. (2)

ϕ	q_0	p	$Q_{0.5}^*$ (J/kg)
Pure water ice			
0.55	45.5	-1.05	73.4
0.37	21.4	-1.02	39.0
0.24	181	-1.62	37.6
0.1	450	-2.18	22.6
Mixture			
0.39	217	-1.75 ^a	32.2
0.38	257	-1.75	35.4
0.26	594	-1.75 ^a	57.2
0.13	1194	-1.75 ^a	85.2
0	1571	-1.75 ^a	99.6

^a In this case only one run (one impact velocity) was performed, so it is impossible to establish a value of parameter p . Therefore, p is assumed to be the same as that for the mixture target with porosity $\phi = 0.38$.

$Q_{0.5}^*$ is defined as Q value for $f_{0.5} = 0.5$, which has a similar physical meaning to Q_s^* . The energy density, $Q_{0.5}^*$, increases from 23 to 73 J/kg when porosity increases from 0.1 to 0.55, as shown in Fig. 12. The empirical relationship between the porosity ϕ and the $Q_{0.5}^*$ is described by the equation

$$Q_{0.5}^* = 20.7(1 - \phi)^{-1.6}. \quad (3)$$

Since $Q_{0.5}^*$ describes fairly well the degree of disruption based on the size distribution, Eq. (3) can be considered a reasonable relation to give the porosity dependence of the impact strength for pure icy targets.

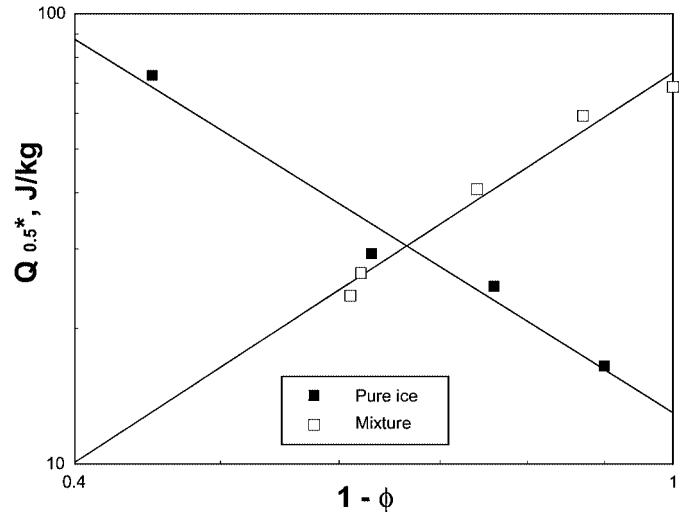


FIG. 12. Porosity dependence of the impact strength defined as the parameter, $Q_{0.5}^*$. The calculated results shown in Table II are shown in the figure and the opposite trends depending on the target type can be seen. The lines are drawn by least-squares fitting for each type of the sample.

3.2.2. Icy-Rocky Mixture

Figure 13 shows the cumulative mass distribution of the fragments for a mixture of targets with porosity 38%. The cumulative mass is found to be almost constant in the fragment region less than some critical value, which varies from 0.001 to 0.01. Such a critical value is found as well in Fig. 10b for the pure icy targets with porosity 55%. The mixture target is quite fragile and is weaker than the pure icy target with the same porosity. Then the same type of disruption as observed for the pure ice target with porosity 55% may occur and it generated separated ice and silicate particles even in the weak compressive stress. We use the same criterion as was used above to determine the impact strength of the mixture target. The normalized fragment mass at $m_c/M_t = 0.5$ is determined for a set of impact velocities in Fig. 13; the result is shown in Fig. 14. We have additional data with other porosities, but there is only one value for each porosity. Nevertheless, they are very useful and sufficient for preliminary analysis of the porosity influence on the impact strength. To derive the impact strength $Q_{0.5}^*$ for the porosity of 38%, Eq. (2) is fitted; the calculated constants q_0 , p , and $Q_{0.5}^*$ are shown in Table II. We assumed the same slope in Eq. (2) to determine $Q_{0.5}^*$ for other porosity data, as shown in Fig. 14 by dashed lines. The estimated $Q_{0.5}^*$ under this assumption is presented together with the experimental value of 38% target in Fig. 12. The relationship between $Q_{0.5}^*$ and porosity can be fit by the equation

$$Q_{0.5}^* = 108(1 - \phi)^{2.3}. \quad (4)$$

We notice that the porosity dependence is completely opposite

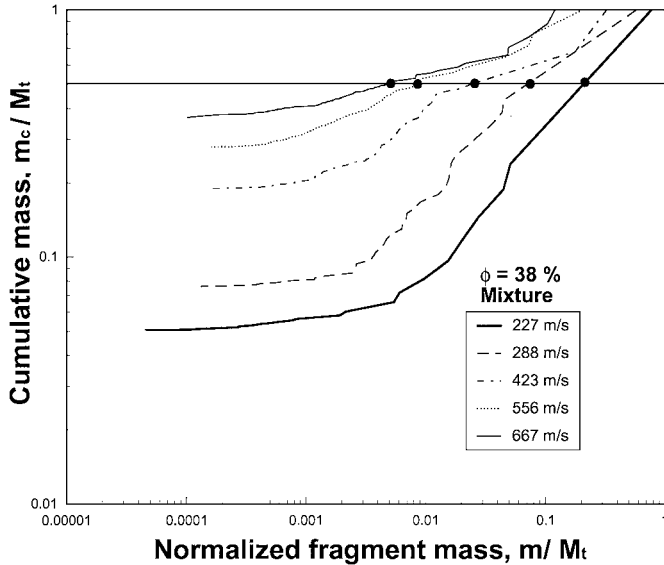


FIG. 13. Size distribution of impact fragments shown by relationship between the cumulative mass and the normalized fragment mass for mixture target with the porosity of 38%. The reference line of $m_c/M_t = 0.5$ is drawn and the cross points with each distribution are shown by the symbols of closed circle. We denote the normalized fragment mass at these cross points as $f_{0.5}$.

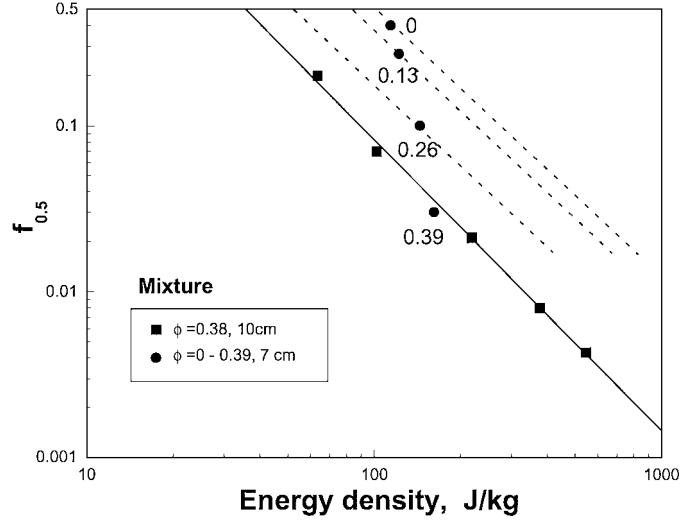


FIG. 14. The relationship between $f_{0.5}$ and energy density for mixture target. The solid line is calculated by least-squares fitting for the data of $\phi = 0.38$, 10 cm. The numbers are the sample porosities for each data in 7-cm target. The dashed lines have the same slope as the solid line and go through each data of 7 cm.

in two types of targets; compare Eqs. (3) and (4). The mixture target shows that the impact strength becomes weaker with the increase in the porosity, but it becomes stronger in the pure icy target. It has been proved that the porous target has an impact strength stronger than that of the non-porous target if the target composition is the same. Our new result for the mixture target is not consistent with previous results for porous targets of different types (Love *et al.* 1993, Ryan *et al.* 1999).

4. DISCUSSION

4.1. Effect of Porosity on the Impact Strength

In the previous section, we found the porosity dependence of two types of targets and showed that the impact strength behaved in a completely opposite direction against the porosity. To understand this curious behavior of the mixture target, we analyze our results by using a scaling law proposed by Mizutani *et al.* (1990). Before we use this scaling law, we should know the basic behavior of the porosity against the fundamental process of the impact disruption, e.g., shock-induced pressure, decay constant of the shock pressure, and static strength of the material. The porosity dependence of the static strength, that is, density dependence, for pure ice was examined by Mellor (1975) in the density range from 150 to 900 kg/m³. The compiled result for compressive strength is interpolated by the power-law equation

$$Y = Y_0(1 - \phi)^n, \quad (5)$$

where $Y_0 = 8.6$ MPa and $n = 4.2$. In Table III, the experimentally fitted coefficients related to Eq. (5) and to some other equations are listed. The shock pressure induced in porous ice

TABLE III
Summary of Equations Fitted to the Experiments and the Appropriate Numerical Parameters

Physical value	Equation	Parameters	Medium	Ref.
Normalized fragment mass versus energy density	(2) $f_{0.5} = q_0 Q^p$	q_0 and p	Ice and icy/mineral mixture	This work, see Table II for details
Energy density corresponding to $f_{0.5} = 0.5$	(3) and (4) $Q_{0.5}^* = a(1 - \phi)^b$	$a = 20.7$ $b = -1.6$ $a = 108$ $b = 2.3$	Ice Icy/mineral mixture	This work This work
Compressive strength Y	(5) $Y = Y_0(1 - \phi)^n$	$Y_0 = 8.6$ MPa $n = 4.2$	Ice	After Mellor (1975)
Shock pressure versus porosity at constant impact velocity	(6) $P_{0\phi} = P_0(1 - \phi)^l$	P_0 $l = 2 \sim 0.7$ for impact velocity 100~5000 m/s $l = 1.5$	Ice-on-ice impacts	After Gaffney (1985) This work, Fig. 15 $P_0/Y_0 = 100$
Shock pressure decay with the distance from an impact point	(7) $P(r) = P_{0\phi}(r_0/r)^m$	$m = 1 \sim 2$ $m = 3 \sim 4$	Crystalline ice Snow	Kato <i>et al.</i> (2001), Arakawa (1999a) Mellor (1977)
Coefficient m appearing in Eq. (7)	(8) $m = m_0(1 - \phi)^k$	$m_0 = 2$ $k = 0.5$	Ice	This work, Fig. 15
Condition for gravitational accumulation of the fragments generated by impact disruption	(13)	Several parameters; also these of Eq. (1)	Icy-silicate porous mixtures	This work, Figs. 16a and 16b
Condition for impact-generated disruption	(14)	Several parameters		

Note. Here “ice” means “water ice” and “icy/mineral mixture” means a mixture with the mass ratio of ice to mineral equal 0.5.

with various porosities was measured and these Hugoniot data were summarized by Gaffney (1985). Then, we can estimate the shock-induced pressure in our impact experiment according to the Hugoniot data under the assumption of the impedance matching method. However, the data for porosity and particle velocity are very limited; there are only two different porosities (62%, 35%), and the available particle velocity is higher than 3000 m/s. Therefore, we should extrapolate and interpolate these data toward the low-velocity region and various porosities, respectively. We imagine that an extrapolation and interpolation procedure is risky, and with the experimental data currently available, we do not see an opportunity to give a reasonable estimate of the size of the uncertainties. The shock pressure at a constant impact velocity can be expressed as

$$P_{0\phi} = P_0(1 - \phi)^l, \quad (6)$$

where P_0 is determined by ice-on-ice impact at each impact velocity according to ice Hugoniot, and l varies with the impact velocity from 2 to 0.7 in the range from 100 to 5000 m/s. In our low-velocity experiment, l could be between 2 and 1.3. The shock pressure decay is usually expressed as

$$P(r) = P_{0\phi} \left(\frac{r_0}{r} \right)^m, \quad (7)$$

where r_0 is the radius of isobaric core and it almost corresponds to the radius of the projectile (r_p), and r is the distance from the impact point. The pressure decay constant m for a non-porous icy target is obtained to be from 1 to 2 by the laboratory experiments of Kato *et al.* (2001) and Arakawa (1999a). The field explosion experiment was used to measure the properties of shock pressure decay in seasonal snow and in ice-sheet snow by Mellor (1977). Then, the decay constant m was derived to be between 3 and 4. These values are larger than that for the non-porous ice and they clearly show that the decay constant depends on the porosity. However, there are no systematic studies to determine the porosity effect on m ; thus we assume that m depends on ϕ as follows:

$$m = m_0(1 - \phi)^{-k}. \quad (8)$$

We choose $m_0 = 2$ and $k = 0.5$. Although this choice is a little bit arbitrary, it leads, through Eq. (8), to the reasonable values of parameter m : They are equal to 2, 2.31, 2.83, and 4 for the porosity equal to 0, 0.25, 0.5, and 0.75, respectively. The endmost values of m of this set are consistent with those found experimentally for non-porous ice (Kato *et al.* 2001, Arakawa 1999a), as well as for high-porous ice (Mellor 1977).

Now we apply the above assumption of the porosity effects to Mizutani’s scaling law for the impact disruption (Mizutani *et al.*

1990). Non-dimensional impact stress (P_I) is the most important parameter to express the degree of impact disruption in Mizutani's model. It is defined as

$$P_I \equiv \frac{P(R)}{Y}, \quad (9)$$

where R is the size of the target; thus the pressure, $P(R)$, corresponds to the antipodal pressure of the impacted target. According to previous results for ice and rocks (e.g., Mizutani *et al.* 1990), when P_I is larger than unity, m_1/M_t is always found to be less than 0.1. So we choose $P_I = 1$ for the impact strength; however, since the impact strength is usually defined as the impact condition to achieve $m_1/M_t = 0.5$, $P_I = 1$ should be considered the upper limit of the strength. By combining Eqs. (5)–(9), we can derive the target size ($R_{P_I=1}$) corresponding to the condition $P_I = 1$,

$$R_{P_I=1} = \left(\frac{P_0}{Y_0} \right)^{1/m} (1 - \phi)^{\frac{l-n}{m}} r_p. \quad (10)$$

Therefore, we can rewrite the energy density showing the impact strength corresponding to $P_I = 1 (Q_{P_I=1})$, by using Eq.(10), as

$$Q_{P_I=1} \equiv \frac{m_P V_i^2 / 2}{M_t} = \frac{1}{2} \frac{r_p^3}{R_{P_I=1}^3 (1 - \phi)} V_i^2, \quad (11)$$

where the projectile and the target are assumed to be made from the same material. Equation (11) is simplified by the normalization with respect to $Q_{P_I=1}$ for $\phi = 0$,

$$\frac{Q_{P_I=1}(\phi)}{Q_{P_I=1}(\phi=0)} = \left(\frac{P_0}{Y_0} \right)^{3\left(\frac{1}{m_0} - \frac{1}{m}\right)} (1 - \phi)^{\frac{3(n-1)-m}{m}}. \quad (12)$$

This equation looks messy, but the physical meaning of each parameter is quite clear. Therefore, we can check the effects of each parameter for the dependencies on the impact strength numerically. Figure 15 shows the porosity dependence of the impact strength calculated by Eq. (12) with the possible values of parameters l , m , n at $P_0/Y_0 = 100$ for pure ice. This numerical value, line A, reproduces the experimental behavior of the porosity dependence of the impact strength of pure ice: the strength increases with increases in porosity. According to Eq. (12), we can recognize that there are several factors enhancing the impact strength of the porous material. The large values of m and l contribute to the increasing dependence in Fig. 15 and the large value of n contributes to the decreasing dependence in Fig. 15. We think that the combination of each parameter in pure ice is accidentally suitable for the dependence in Fig. 15; probably the large m of high-porosity target determines this tendency. The decreasing dependence in Fig. 15 could be reproduced easily by changing the parameter n to a larger value. The numerical calculation of this idea is

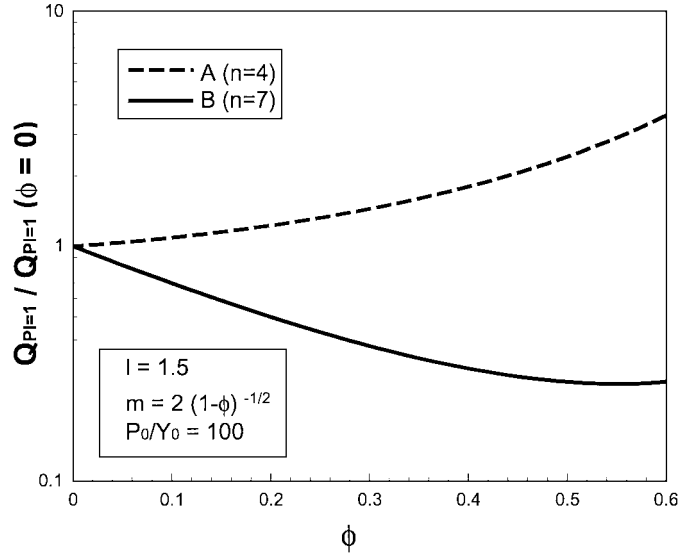


FIG. 15. Empirical relationship between the porosity and the normalized impact strength according to Eq. (12): Calculations were performed for $l = 1.5$, $m = 2(1 - \phi)^{-1/2}$, and $P_0/Y_0 = 100$. Two values of parameter n were used: Line A is calculated with $n = 4$ corresponding to the trend of pure ice target. Line B is calculated with $n = 7$ and its trend is the same as for the mixture target. The large n value may be the reason that the mixture has a curious behavior in the impact strength with the porosity.

shown in Fig. 15, line B, in which we only changed n from 4 to 7; other parameters are the same for both lines A and B. The calculated line B decreases with increases in porosity, as predicted above. This result strongly suggests that the mechanism causing the curious behavior of the mixture target may be explained by the strong dependence of the static strength of the mixture target on the porosity. Of course, there is another possible way to explain the trend in Fig. 15 by using the other values of the parameters l , m_0 , and k . Unfortunately we do not have static strength data and other necessary parameters of the mixture target to check this idea. In the future, it is necessary to study it together with the measurement of the decay constant and the shock-induced pressure in the mixture target with variable porosities.

4.2. Implication for Collisions of Icy Bodies in the Solar System

The impact conditions for accumulation of small icy bodies are discussed on the basis of our experimental results, Eqs. (1), (3), and (4). When two bodies collide at high impact velocity, they disrupt into small fragments and these fragments are ejected from these bodies. However, if the colliding bodies are massive enough, their gravity field attracts these ejected fragments. We can estimate whether impact fragments can accumulate on the target body or not by comparing the ejecta velocity with the escape velocity of the target body. The following equation gives the accumulation condition of the impact fragments, which is simply derived from comparing Eq. (1) with the escape velocity

of the target body,

$$V_{i-\text{acc}} \leq \frac{\left(\frac{8}{3}\pi G\rho(1-\phi)\right)^{1/2}}{-2.17\phi + 1.29} R, \quad (13)$$

where $V_{i-\text{acc}}$ is the maximum impact velocity able to capture all of the impact fragments by the gravitational attraction force, ρ is the density of the target body related to its non-porous state, and R is the radius of the target body. Equation (13) is valid when one body is smaller than the other. We assume that the smaller body is a non-porous pure ice body in order to use our results directly in the following considerations. Figure 16a and 16b show the calculated results of Eq. (13) to show the porosity dependence of the accumulation condition for the bodies with a radius of 100 km. Two types of bodies are shown in Fig. 16: pure icy body (a) and mixture body (b), with its composition similar to that in this experiment. The accumulation condition is in a region below the solid lines. The impact velocity for accumulation decreases from more than 500 m/s to as low as 60 m/s with a decrease in porosity. There is a small difference between a pure ice (a) and mixture (b) body: the mixture shows a slightly higher velocity for accumulation since the non-porous density of the mixture is higher than that of pure ice.

The impact condition for the disruption of small bodies can be estimated from Eqs. (3) and (4) if we ignore the size effect on the mechanical strength. However, the size effect has been studied and discussed to extrapolate the laboratory data to the real size body. Theoretical and laboratory studies have been conducted to clarify this effect and recently numerical simulation was also used (Housen and Holsapple 1990, Nolan *et al.* 2001). However, this issue is still a controversial and an ongoing problem. Thus, we adopt the simplest assumption that the mechanical strength is a constant value, irrespective of the size. The derived equation to show the disruption condition is

$$V_{i-\text{dis}} \geq \left[2a(1-\phi)^{b+1} \frac{\rho}{\rho_i} \left(\frac{R}{r_p} \right)^3 \right]^{1/2}. \quad (14)$$

Here a , b are the constants that appear in Eq. (3) for pure ice ($a = 20.7$, $b = -1.6$) and in Eq. (4) for the mixture ($a = 108$, $b = 2.3$). Density ρ denotes the non-porous density of material forming the larger body (target with radius R). The density of the smaller body (impactor with radius r_p) is assumed to be equal to that of non-porous water ice $\rho_i = 917 \text{ kg/m}^3$. When we choose $R/r_p = 5$, the porosity dependence of the disruption condition for pure ice and for mixture is shown in Figs. 16a and 16b by dashed lines. The impact velocity required for the disruption increases with increases in porosity for pure ice, but it behaves conversely for the mixture body.

We can predict what happens as a result of the collision by combining Eqs. (13) and (14). Figure 16 is now regarded as a collisional event diagram for the pure ice body (a) and mixture body (b). Each diagram is divided into three regions: mass loss, rubble pile formation, and regolith formation (compaction). The

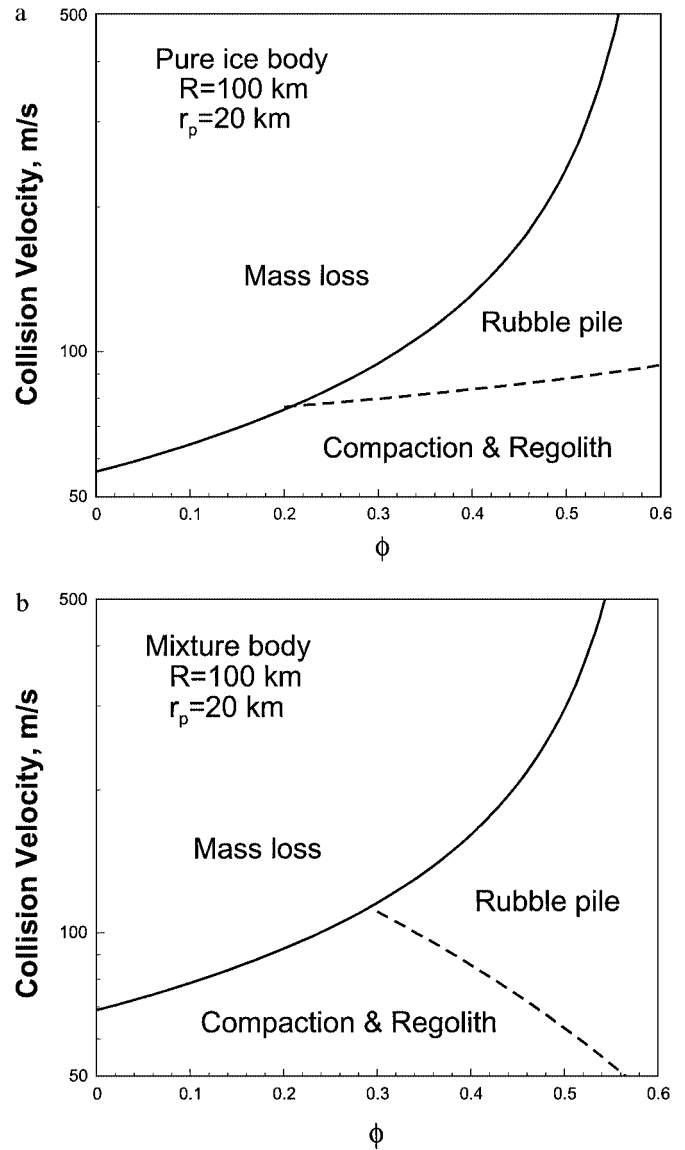


FIG. 16. Collisional event map for pure ice body (a) and mixture body (b). A solid line in each part is the boundary to show the accumulation condition calculated from Eq. (13). A dashed line in each part is the boundary of the impact disruption calculated from Eq. (14). The colliding bodies are assumed to have the size of 100 and 20 km. The non-porous density of pure ice and mixture body is 917 and 1370 kg/m^3 , respectively. The impact condition is divided into three regions according to the resultant of the collisional event. They are mass loss, rubble pile formation, and compaction and regolith formation.

mass loss region is considered to be a higher velocity region than the boundary determined by the accumulation condition; some amounts of the impact fragments escape from the target body. The rubble pile region corresponds to the region between the accumulation and disruption boundaries. Therefore, the target body is considered to break completely once, and then its fragments reaccumulate to form a rubble pile body by the gravitational attraction force. The regolith formation (compaction) region is the region of accumulation and no disruption. In this

condition, the impacts form only craters on the surface and the excavated ejecta fly away from the target body. But the ejecta velocity is too small to escape from the gravity field of the target body, thus allowing reaccumulation on the surface to form a regolith layer. In this region, when the porosity of the target body is very large, it could be possible to form a crater by compaction of a porous layer but not by the excavation of the surface. This compaction mechanism is quite effective to capture the impact-ing material.

We notice that the compaction and regolith region is dominant in pure ice target at low collision velocity, and the region to form the rubble pile body exists above that region. The rubble pile region becomes very narrow quickly with decreases in porosity. On the other hand, in the mixture body, the rubble pile and the compaction and regolith formation region equally exist. The important property is that the rubble pile region only appears in the high porosity region for the mixture body; in contrast, that region extends through the lower porosity in pure ice body. This difference in the collisional event may affect the internal evolution of small icy bodies.

ACKNOWLEDGMENTS

We are grateful to the reviewers, Dr. S. Love and Dr. D. R. Davis, for their very detailed study of the manuscript and their constructive remarks. Our extreme gratitude is extended to Professor A. Kouchi, Dr. S. Yamamoto, and Dr. N. Watanabe of Institute of Low Temperature Science, Hokkaido University, for their useful discussions of these experiments. We also thank S. Nakatsubo, S. Matsumoto, and T. Segawa of the Contribution Division of Institute of Low Temperature Science, Hokkaido University, for their technical help with the experiments. This work was supported by a grant-in-aid for scientific research (Grant 13440156) from the Japan Ministry of Education, Science, Sports and Culture. The research visit of J.K.L. to Hokkaido University was supported by the Japan Society for the Promotion of Sciences within the frame of the bilateral cooperation with the Polish Academy of Sciences.

REFERENCES

- Arakawa, M. 1999a. Collisional disruption of ice by high-velocity impact. *Icarus* **142**, 34–45.
- Arakawa, M. 1999b. Ejection velocities of ice fragments in oblique impacts of ice spheres. *Adv. Space Res.* **23**, 1217–1224.
- Arakawa, M., and M. Higa 1996. Measurements of ejection velocities in collisional disruption of ice spheres. *Planet. Space Sci.* **44**, 901–908.
- Arakawa, M., N. Maeno, M. Higa, Y. Iijima, and M. Kato 1995. Ejection velocity of ice impact fragments. *Icarus* **118**, 341–354.
- Arakawa, M., M. Higa, J. Leliwa-Kopystynski, and N. Maeno 2000. Impact cratering of granular mixture targets made of H₂O ice–CO₂ ice–pyrophyllite. *Planet. Space Sci.* **48**, 1437–1446.
- Asphaug, E., S. J. Ostro, R. S. Hudson, D. J. Scheeres, and W. Benz 1998. Disruption of kilometer-sized asteroids by energetic collisions. *Nature* **393**, 437–440.
- Britt, D. T., and G. J. Consolmagno 2001. Modeling the structure of high porosity asteroids. *Icarus* **152**, 134–139.
- Davis, D. R., and E. V. Ryan 1990. On collisional disruption: Experimental results and scaling law. *Icarus* **83**, 156–182.
- Eluszkiewicz, J., J. Leliwa-Kopystynski, and K. J. Kossacki 1998. Metamorphism of Solar System ices. In *Solar System Ices* (B. Schmitt, C. de Bergh, and M. Festou, Eds.), pp. 119–138. Kluwer Academic, Dordrecht/Norwell, MA.
- Fujiwara, A., G. Kamimoto, and A. Tsukamoto 1977. Destruction of basaltic bodies by high-velocity impact. *Icarus* **31**, 277–288.
- Fujiwara, A., T. Kadono, and A. Nakamura 1993. Cratering experiments into curved surfaces and their implication for craters on small satellites. *Icarus* **105**, 345–350.
- Gaffney, E. S. 1985. Hugoniot of water ice. In *Ices in the Solar System* (J. Klinger, D. Benest, A. Dollfus, and R. Smoluchowski, Eds.), pp. 119–148. Reidel, Dordrecht.
- Housen, K. R., and K. A. Holsapple 1990. On the fragmentation of asteroids and planetary satellites. *Icarus* **84**, 226–253.
- Housen, K. R., K. A. Holsapple, and M. E. Voss 1999. Compaction as the origin of the unusual craters on the asteroid Mathilde. *Nature* **402**, 155–157.
- Kato, M., Y. Iijima, M. Arakawa, Y. Okimura, A. Fujimura, N. Maeno, and H. Mizutani 1995. Ice-on-ice impact experiments. *Icarus* **113**, 423–441.
- Kato, M., M. Higa, K. Shirai, Y. Iijima, T. Kiyono, S. Nakazawa, and M. Arakawa 2001. Shock pressure attenuation in water ice at a pressure below 1 GPa. *J. Geophys. Res.* **106**, 17,567–17,578.
- Kawakami, S., H. Mizutani, Y. Takagi, M. Kato, and M. Kumazawa 1983. Impact experiments on ice. *J. Geophys. Res.* **88**, 5806–5814.
- Kawakami, S., Y. Kanaori, A. Fujiwara, M. Arakawa, M. Kato, H. Mizutani, P. Cerroni, and F. Capaccioni 1991. An experimental study of impact fracturing of small planetary bodies in the Solar System with an application to Phobos. *Astron. Astrophys.* **241**, 233–242.
- Kossacki, K. J., N. I. Kömle, J. Leliwa-Kopystynski, and G. Kargl 1997. Laboratory investigation of the evolution of cometary analogs: Results and interpretation. *Icarus* **128**, 127–144.
- Lange, M., and T. J. Ahrens 1983. The dynamic tensile strength of ice and ice-silicate mixtures. *J. Geophys. Res.* **88**, 1197–1208.
- Lange, M., and T. J. Ahrens 1987. Impact experiments in low-temperature ice. *Icarus* **69**, 506–518.
- Leliwa-Kopystynski, J., and K. J. Kossacki 2000. Evolution of porosity in small icy bodies. *Planet. Space Sci.* **48**, 727–745.
- Love, S. G., F. Hörz, and D. E. Brownlee 1993. Target porosity effects in impact cratering and collisional disruption. *Icarus* **105**, 216–224.
- Mellor, M. 1975. A review of basic snow mechanics. *IAHS-AISH Publ.* **114**, 251–291.
- Mellor, M. 1977. Engineering properties of snow. *J. Glaciol.* **81**, 15–66.
- Melosh, H. J. 1989. *Impact Cratering*. Oxford Univ. Press, Oxford.
- Melosh, H. J., and E. V. Ryan 1997. Asteroids: Shattered but not dispersed. *Icarus* **129**, 562–564.
- Mizutani, H., Y. Takagi, and S. Kawakami 1990. New scaling law on impact fragmentation. *Icarus* **87**, 307–329.
- Nolan, M. C., E. Asphaug, R. Greenberg, and H. J. Melosh 2001. Impact on asteroids: Fragmentation, regolith transport, and disruption. *Icarus* **153**, 1–15.
- Rickman, H. 1998. Composition and physical properties of comets. In *Solar System Ices* (B. Schmitt, C. De Bergh, and M. Festou, Eds.), pp. 395–417. Kluwer Academic, Dordrecht.
- Ryan, E. V., D. R. Davis, and I. Giblin 1999. A laboratory impact study of simulated Edgeworth–Kuiper belt objects. *Icarus* **142**, 56–62.
- Takagi, Y., H. Mizutani, and S. Kawakami 1984. Impact fragmentation experiments of basalt and pyrophyllites. *Icarus* **59**, 462–477.